Formation, Thermodynamic Structure, and Airflow of a Japan Sea Polar Airmass Convergence Zone

TYLER K. WEST[a] AND W. JAMES STEENBURGH[a]

[a] *Department of Atmospheric Sciences, University of Utah, Salt Lake City, Utah*

(Manuscript received 27 April 2021, in final form 11 November 2021)

ABSTRACT: The Sea of Japan (SOJ) coast and adjoining orography of central Honshu, Japan, receive substantial snowfall each winter. A frequent contributor during cold-air outbreaks (CAOs) is the Japan Sea polar airmass convergence zone (JPCZ), which forms downstream of the highland areas of the Korean Peninsula (i.e., the Korean Highlands), extends southeastward to Honshu, and generates a mesoscale band of precipitation. Mesoscale polar vortices (MPVs) ranging in horizontal scale from tens (i.e., meso-β-scale cyclones) to several hundreds of kilometers (i.e., "polar lows") are also common during CAOs and often interact with the JPCZ. Here we use satellite imagery and Weather Research and Forecasting Model simulations to examine the formation, thermodynamic structure, and airflow of a JPCZ that formed in the wake of an MPV during a CAO from 2 to 7 February 2018. The MPV and its associated warm seclusion and bent-back front developed in a locally warm, convergent, and convective environment over the SOJ near the base of the Korean Peninsula. The nascent JPCZ was structurally continuous with the bent-back front and lengthened as the MPV migrated southeastward. Trajectories illustrate how air–sea interactions and flow splitting around the Korean Highlands and channeling through low passes and valleys along the Asian coast affect the formation and thermodynamic structure of the JPCZ. Contrasts in airmass origin and thermodynamic modification over the SOJ affect the cross-JPCZ temperature gradient, which reverses in sign along the JPCZ from the Asian coast to Honshu. These results provide new insights into the thermodynamic structure of the JPCZ, which is an important contributor to hazardous weather over Japan.

KEYWORDS: Snowbands; Topographic effects; Snow; Winter/cool season; Air–sea interaction

1. Introduction

Some of the largest cool-season snowfalls and deepest seasonal snowpacks observed on Earth occur near the Sea of Japan (SOJ) coast of Japan (Takahashi et al. 2013). In the Hokuriku region along the SOJ coast of central Honshu (see Fig. 1 for geographic locations), the low-elevation city of Joetsu averages 635 cm of snow annually and snow depths in nearby mountain areas can reach 7 m (Yamaguchi et al. 2011; Steenburgh 2014; Steenburgh and Nakai 2020). This copious and frequent snowfall stimulates a vibrant winter-sports economy and provides regional water resources, but also creates transportation, structural, and other hazards due to icy roads, snow loading, and avalanches (Eito et al. 2005; Nakai et al. 2012).

Most of this snowfall comes from sea-effect precipitation (e.g., Magono et al. 1966; Tsuchiya and Fujita 1967; Nakai et al. 2005; Eito et al. 2010; West et al. 2019; Veals et al. 2019), which is comparable to lake-, sea-, and ocean-effect precipitation in other regions of the world (e.g., Andersson and Nilsson 1990; Niziol et al. 1995; Steenburgh et al. 2000; Laird et al. 2009; Kindap 2010; Norris et al. 2013; Veals and Steenburgh 2015; Kristovich et al. 2017). Over Japan, such precipitation develops during the East Asian winter monsoon, which features anticyclonic flow around the semipermanent Siberian high and frequent cold-air outbreaks (CAOs) over the warm waters of the SOJ (Mitnik 1992; Dorman et al. 2004). During CAOs, strong sensible and latent heat fluxes over the SOJ lead to the generation of clouds and precipitation that are enhanced near the Japanese coast and adjoining mountains (e.g., Kawamoto et al. 1963; Higuchi 1963; Magono 1971; Estoque and Ninomiya 1976; Nakai and Endoh 1995; Saito et al. 1996; Yoshihara et al. 2004; Kusunoki et al. 2005; Campbell et al. 2018; Veals et al. 2019; West et al. 2019).

During some CAOs, sea-effect precipitation becomes organized over the western SOJ into a broader, mesoscale band of clouds and precipitation known as the Japan Sea polar airmass convergence zone (JPCZ; Okabayashi 1969; Endoh et al. 1984; Asai 1988; Murakami 2019). The JPCZ can produce heavy snow in the Hokuriku and other regions of southwest Honshu (Okabayashi and Satomi 1971; Hozumi and Magono 1984; Endoh et al. 1984; Nagata et al. 1986) and forms in response to flow interactions with the highland areas of the Korean Peninsula (the Changbai, Jangbaek, Ohnan, or Šanggiyan Mountains, hereinafter simply called the Korean Highlands), the thermal contrast between the Korean Peninsula and the SOJ, and the sea surface temperature distribution of the SOJ (Nagata et al. 1986; Nagata 1991; Shinoda et al. 2021). The JPCZ typically develops near the base of the Korean Peninsula and extends southeast toward Honshu, most frequently intersecting the SOJ coast between Matsue and Joetsu (see Fig. 1) (Uemura 1980; Endoh et al. 1984; Ohigashi and Tsuboki 2007; Eito et al. 2010). As highlighted by Murakami (2019), debate persists concerning the thermal structure of the JPCZ, with previous studies indicating colder air to the southwest, colder

---

Corresponding author: W. James Steenburgh, jim.steenburgh@utah.edu

DOI: 10.1175/MWR-D-21-0095.1

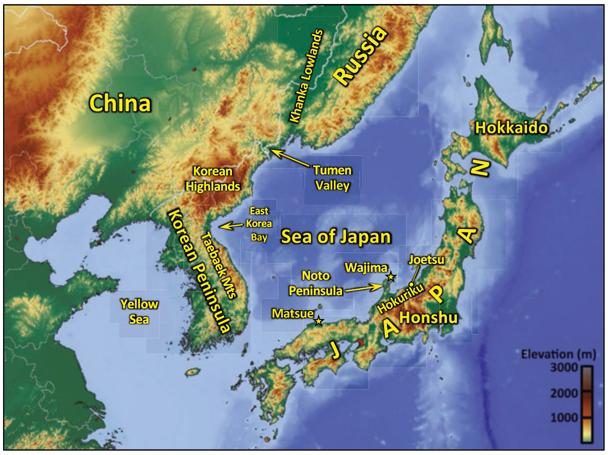

FIG. 1. Topography [in meters above mean sea level (MSL), shaded following the inset scale] and geographic landmarks of the study region. Stars indicate the Matsue and Wajima sounding locations. (Adapted from https://maps-for-free.com/.)

air to the northwest, or a weak thermal contrast or warm-tongue structure (Hozumi and Magono 1984; Nagata 1987, 1992). Nagata (1992) suggests that this cross-JPCZ temperature structure modulates the intensity, location, and structure of the convective cloud band and other cloud features accompanying the JPCZ.

The JPCZ may share some similarities with terrain or thermally driven mesoscale lake- and sea-effect bands in other regions of the world. For example, thermally forced land breezes, orographically induced convergence, and coastline geometry can lead to mesoscale precipitation bands over the Great Lakes, the Great Salt Lake, Lake Constance, and the Baltic Sea (e.g., Andersson and Gustafsson 1994; Alcott et al. 2012; Umek and Gohm 2016; Steenburgh and Campbell 2017). Among the most intense are long-lake-axis parallel bands over elongated bodies of water such as Lake Ontario (e.g., Passarelli and Braham 1981; Steiger et al. 2013; Kristovich et al. 2017; Campbell and Steenburgh 2017). Such bands often feature a cross-band secondary circulation that organizes and intensifies precipitation (Bergmaier et al. 2017).

During individual events, the position of the JPCZ fluctuates with the passage of upper-level troughs, mesoscale polar vortices (MPVs), and other large-scale features (Endoh et al. 1984; Nagata 1993; Ohigashi and Tsuboki 2007). MPVs occur frequently during CAOs, span horizontal dimensions from tens of kilometers to several hundred kilometers, and can produce heavy snowfall and damaging winds (Asai 1988; Ninomiya 1989; Ogura 1991; Nagata 1993; Fu et al. 2004; Murakami 2019; Watanabe et al. 2016, 2018). MPVs are observed over other mid- and high-latitude bodies of water (e.g., Sardie and Warner 1985; Rasmussen and Lystad 1987; Businger and Walter 1988), including the Great Lakes (e.g., Laird et al. 2003; Steiger et al. 2013), and are sometimes referred to as *polar lows* when their horizontal dimensions are ≥ 200 km (Rasmussen and Turner 2003; Ninomiya 1989) or *meso-β-scale vortices* when their horizontal dimensions are smaller (Nagata 1993; Tsuboki and Asai 2004). We use the general phrase MPV to be inclusive of a wide range of horizontal scales and the occasional upscale growth of meso-β-scale vortices into polar lows.

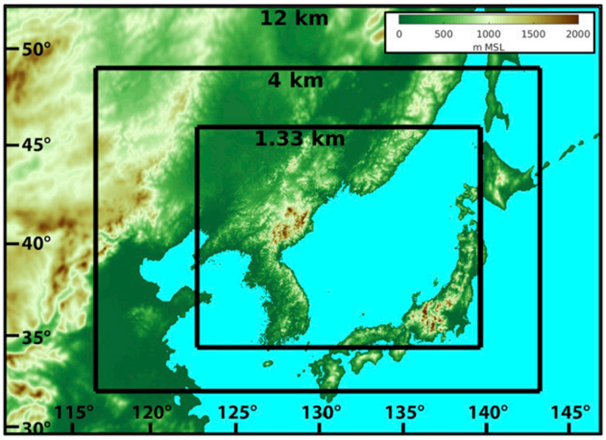

FIG. 2. WRF domains and topography (m MSL from the highest-resolution domain, shaded following the inset scale).

MPVs form poleward of the polar front under the influence of cold upper-level troughs (Reed 1979; Rasmussen and Turner 2003; Shimada et al. 2014). Over the SOJ, many MPVs form downstream of the Korean Highlands and move southeastward along a path similar to that of the JPCZ, often impacting the Hokuriku region (Asai 1988; Tsuboki and Asai 2004; Watanabe et al. 2016; Yanase et al. 2016). Smaller meso-β-scale vortices can also form in conjunction with larger MPVs or along a well-developed JPCZ (Nagata 1993; Tsuboki and Asai 2004). Factors that aid MPV formation and maintenance over the SOJ or the development of meso-β-scale vortices along the JPCZ include strong surface sensible and latent heat fluxes, latent heating from convection, shear instability, and baroclinic instability (Tsuboki and Wakahama 1992; Nagata 1993; Yanase et al. 2002; Kawashima and Fujiyoshi 2005; Føre et al. 2012).

In this paper we examine the formation, thermodynamic structure, and airflow of a JPCZ during a multiday CAO from 2 to 7 February 2018, focusing on the influence of an MPV, the modification of airflows by the Korean Highlands, and the contributions of airmass origin and air–sea interactions to the JPCZ thermal structure. The event produced heavy snow in the Fukui and Ishikawa Prefectures, including 146 cm in Fukui City, with people trapped for as many as two nights in vehicles along major highways (Kyodo News 2018). Using higher-resolution modeling and a longer simulation period, we illustrate the JPCZ structure, airmass origins, and airflow in greater detail than previous studies. We describe our data and methods in section 2 and provide a synoptic overview of the event in section 3. We make extensive use of a numerical simulation by the Weather Research and Forecasting (WRF) Model, which is validated in section 4. Section 5 illustrates the formation of the JPCZ in the wake of the MPV, while section 6 diagnoses the thermodynamic structure and airflow of the mature

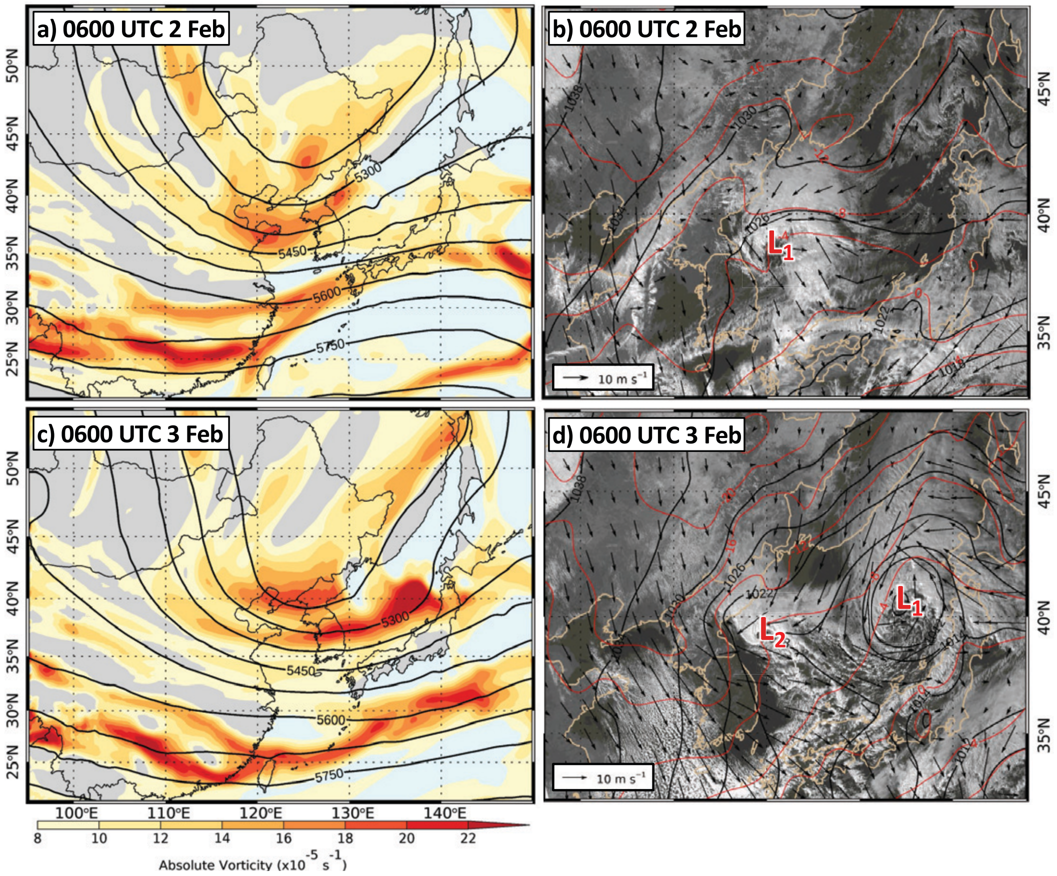

FIG. 3. (a),(c) ERA5 500-hPa geopotential height (contours every 75 m) and absolute vorticity (shaded following the scale at bottom left) and (b),(d) *Himawari-8* visible satellite imagery and ERA5 850-hPa winds (vectors following the inset scale), 850-hPa temperature (red contours every 4°C), and sea level pressure (black contours every 4 hPa) at (top) 0600 UTC 2 Feb and (bottom) 0600 UTC 3 Feb. MPV1 and MPV2 are identified with L1 and L2, respectively.

JPCZ including variations in the cross-JPCZ thermal contrast. Conclusions are summarized in section 7.

2. Data and methods

Satellite imagery and regional analyses used to describe the observed event and validate WRF simulations come from the Japanese *Himawari-8* geostationary satellite, the ERA5 reanalysis (Hersbach et al. 2020), and Japan Meteorological Agency upper-air sounding sites at Matsue and Wajima (Fig. 1). We obtained the *Himawari-8* imagery from the University of Wisconsin–Madison Space Science and Engineering Center (SSEC 2018) and the ERA5 reanalysis from the ECMWF climate data store (Copernicus Climate Change Service 2017). The ERA5 provides hourly reanalyses at 31-km horizontal grid spacing, although we present only selected times and use data on a 0.25° latitude–longitude grid. We obtained the upper-air soundings from the University of Wyoming database (University of Wyoming 2018).

We simulate the 2–7 February 2018 (the year hereinafter is 2018 unless otherwise noted) CAO using the Advanced Research version of WRF, version 4.0 (Skamarock and Klemp 2008). WRF was initialized at 1200 UTC 2 February, 24 h prior to the JPCZ formation, and run through 1200 UTC 7 February, although we focus our analysis on the JPCZ formation and structure at maturity (i.e., through 0600 UTC 5 February for detailed analysis and 1200 UTC 5 February for comparison with observed soundings). The simulation uses three one-way nested domains at 12-, 4-, and 1.33-km grid spacing. The innermost 1.33-km model domain was sufficiently large to include the Korean Highlands, the Korean Peninsula, western and central SOJ, and nearly all the Honshu SOJ coast (Fig. 2). Forty terrain-following half-η levels were used with the greatest resolution within the boundary layer and a 5-km-deep Rayleigh damping layer at the upper boundary. Initial atmospheric conditions, land surface conditions, sea surface temperatures, sea ice coverage, and snow coverage come from the National Centers for Environmental Protection (NCEP) Global Forecast System (GFS) global analysis on a 0.25° latitude–longitude grid (NCEP 2015). The 6-hourly lateral boundary conditions also derive from GFS analyses. Land-use characteristics and topography

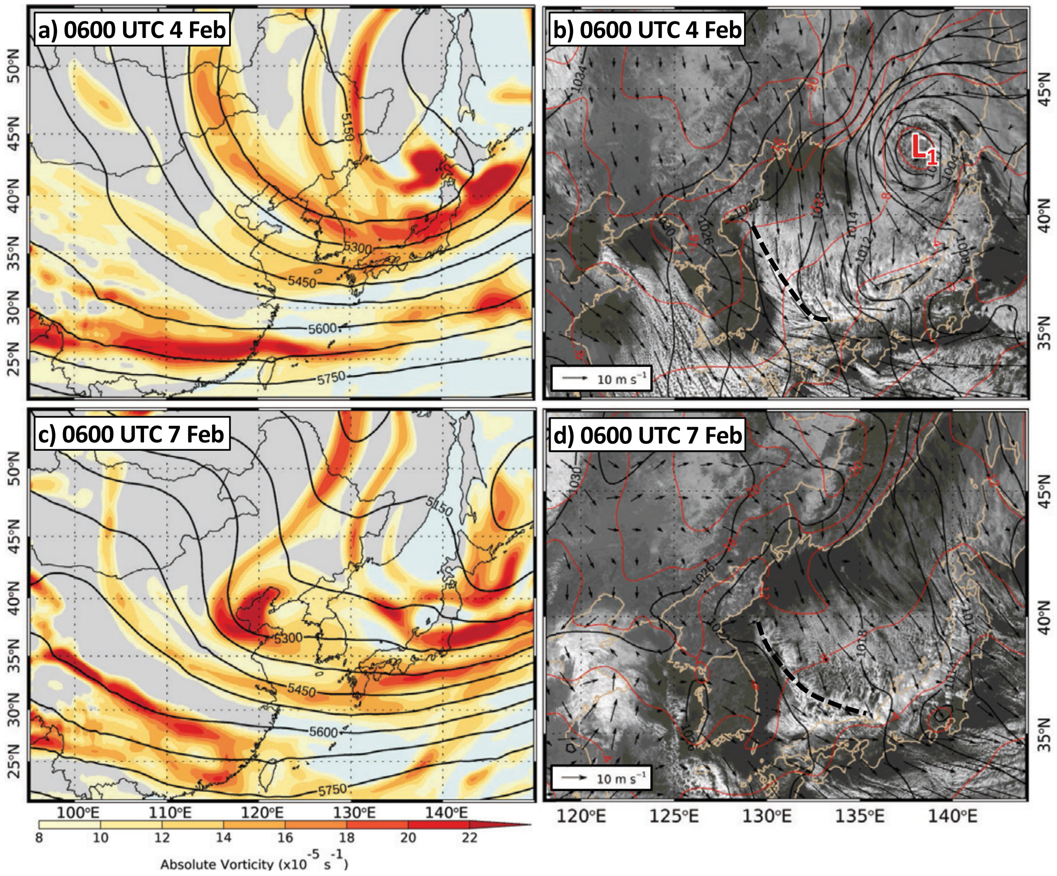

FIG. 4. As in Fig. 3, but for (a),(b) 0600 UTC 4 Feb and (c),(d) 0600 UTC 7 Feb; JPCZ is identified with a black dashed line.

come from the standard WRF Preprocessing System, version 4.0, geographical input data, which rely heavily on Moderate Resolution Imaging Spectroradiometer (MODIS) imagery. Despite being based on a relatively coarse 0.25° grid, initial sea surface temperature and snow-cover analyses compared favorably to operational sea surface temperature and MODIS snow-cover imagery and were deemed sufficient, with the former used throughout the simulation. On the basis of physics suites that have proven successful in previous lake- and sea-effect simulations (e.g., Alcott and Steenburgh 2013; McMillen and Steenburgh 2015a,b; Campbell et al. 2018; Veals et al. 2020), we used the Yonsei University planetary boundary layer scheme (Hong et al. 2006), Thompson cloud microphysics scheme (Thompson et al. 2008), Noah land surface model (Chen and Dudhia 2001), Dudhia shortwave radiation scheme (Dudhia 1989), revised MM5 surface layer parameterization (Jiménez et al. 2012), Rapid Radiative Transfer Model (for longwave radiation; Iacono et al. 2008), and the Kain–Fritsch 2 cumulus parameterization (Kain 2004). The former was used only for the 12-km domain, with the 4- and 1.33-km domains being convection permitting.

Three-dimensional trajectories are calculated with second-order, semi-implicit discretization from 10-min model output from the 1.33-km domain using open-source Python code described by Gowan (2019), which is based on techniques described in Miltenberger et al. (2013; see their section 2.1). In addition to trajectory paths, we present potential temperature, boundary layer and radiation (longwave and shortwave) scheme heating rates, and cloud microphysics scheme heating rates to illustrate processes along trajectories. The boundary layer and radiation scheme heating rates are combined for brevity, with contributions from the latter typically largest along trajectories on the lowest model level over the Sea of Japan where longwave emissions from the relatively warm water surface are absorbed by water vapor in the cold overlying air mass.

3. Synoptic overview

The 2–7 February CAO featured a JPCZ that formed over the western SOJ in the wake of two MPVs. The first MPV (hereinafter MPV1) formed near the East Korean Bay as an upper-level trough approached the western SOJ at 0600 UTC 2 February (Figs. 3a,b). Over the next 24 h, MPV1 moved eastward and northeastward, growing in horizontal scale, and by 0600 UTC 3 February was centered off the northern SOJ coast of Honshu (Fig. 3d). A second upper-level shortwave trough and associated absolute-vorticity maximum began to move over the SOJ at this time and, along with the development of low-level

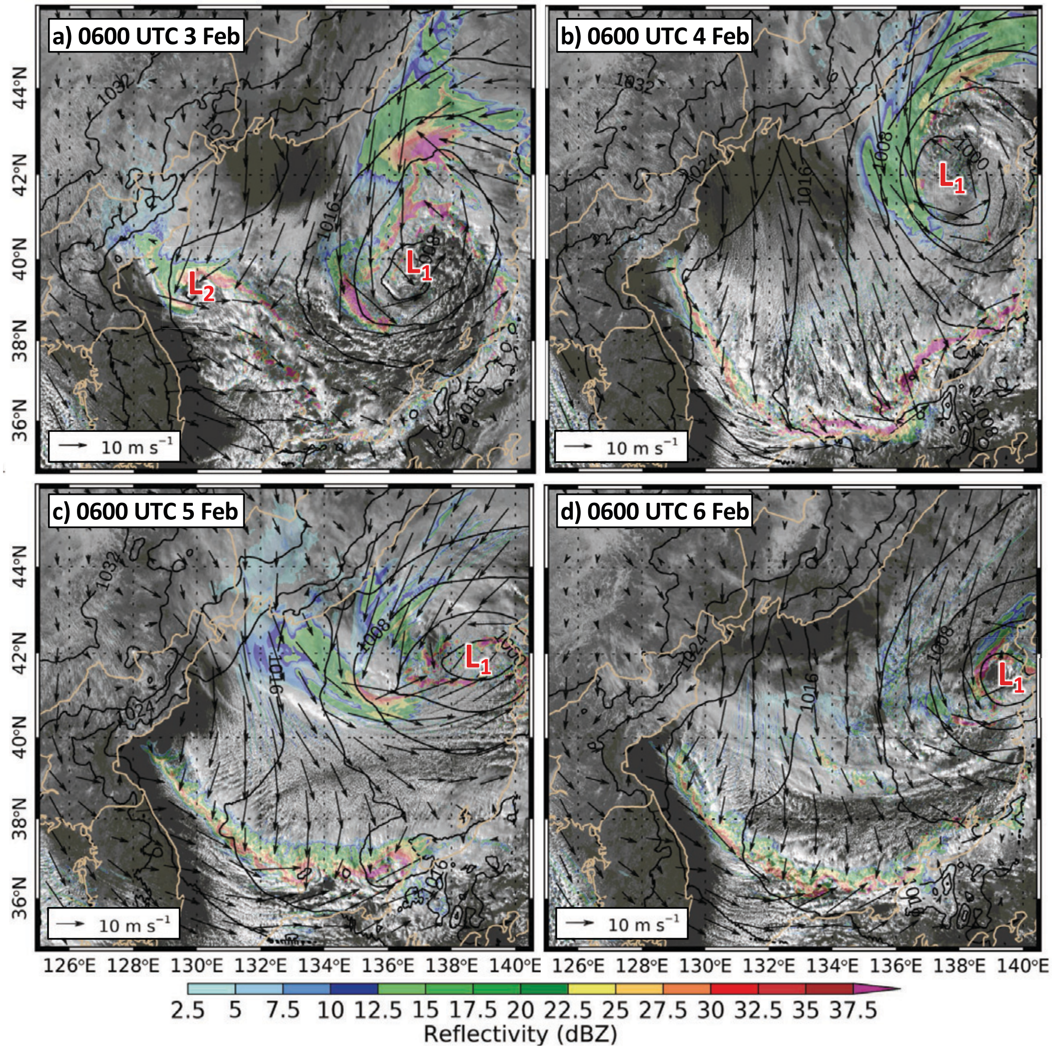

FIG. 5. *Himawari-8* visible satellite imagery, WRF lowest half-η-level radar reflectivity (shaded following the scale at bottom), WRF sea level pressure (black contours every 4 hPa), and WRF lowest half-η-level winds (vectors following the inset scale) at (a) 0600 UTC 3 Feb, (b) 0600 UTC 4 Feb, (c) 0600 UTC 5 Feb, and (d) 0600 UTC 6 Feb. MPV1 and MPV2 are identified with L1 and L2, respectively.

flow across the Korean Highlands, led to the development of a second MPV (hereinafter MPV2) over the western SOJ (Figs. 3c,d).

The upper-level trough progressed eastward through 0600 UTC 4 February with MPV1 deepening near the southwest coast of Hokkaido Island (Figs. 4a,b). Over the western SOJ, temperatures decreased ~4°C in response to cold air advection (cf. Figs. 3d and 4b) and MPV2 moved southeastward toward Honshu where it dissipated near the Noto Peninsula at ~0400 UTC 4 February (not shown). By 0600 UTC 4 February, the JPCZ that developed in the wake of MPV2 extended from the coastal area downstream of the Korean Highlands to the Honshu coast (Fig. 4b). Conditions during this period featured large-scale, low-level, northerly to northwesterly flow that interacted with the Korean Highlands and permeated the western SOJ (Fig. 4b). This synoptic environment persisted through ~0600 UTC 7 February, when the upper-level flow became more zonal and the JPCZ began to weaken (Figs. 4c,d). The intersection of the JPCZ with the Honshu SOJ coast varied between ~133° and ~137°E during the event (e.g., Figs. 4b,d).

4. Model validation

Given the paucity of in situ observations over the SOJ, we first validate the WRF simulation through comparison with *Himawari-8* visible satellite imagery. Overlays of simulated sea level pressure, lowest half-η-level wind vectors, and lowest half-η-level radar reflectivity on *Himawari-8* imagery indicate that WRF captures well the structure and evolution of MPV1, MPV2, and the JPCZ (Fig. 5). At 0600 UTC 3 February, the WRF sea level pressure,

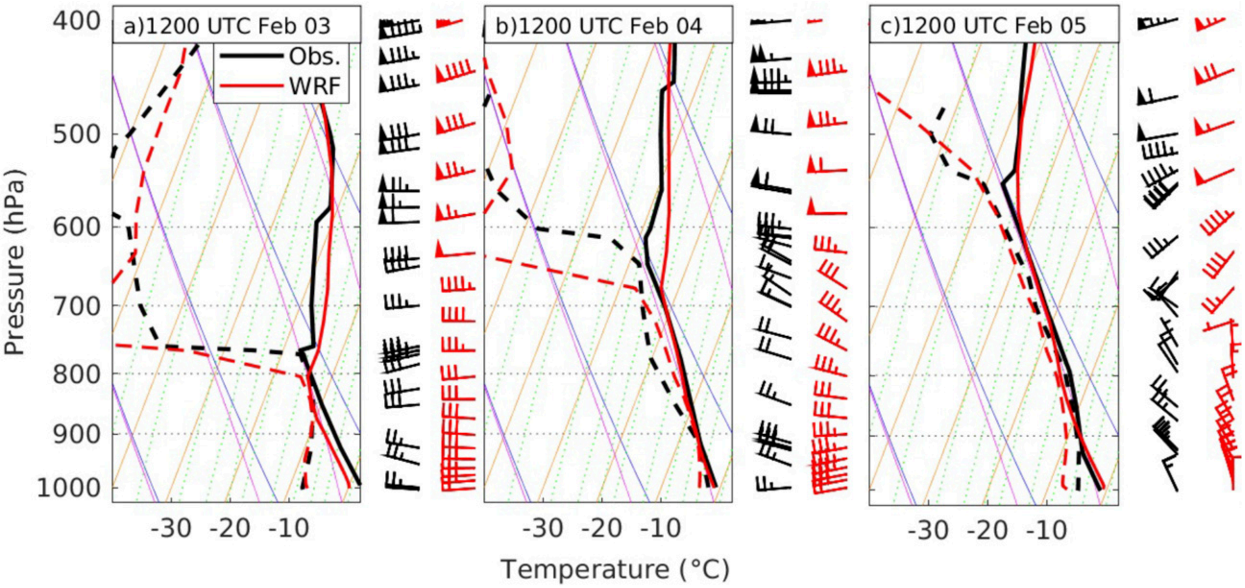

FIG. 6. Observed (black) and WRF (red) skew *T*–log*p* diagrams: temperature (°C; solid), dewpoint (°C; dashed), and wind barbs (full and half barbs denote 5 and 2.5 m s^{-1}, respectively), for (a) Matsue at 1200 UTC 3 Feb, (b) Matsue at 1200 UTC 4 Feb, and (c) Wajima at 1200 UTC 5 Feb.

wind, and radar reflectivity fields are consistent with the observed MPV1 cloud pattern in the eastern SOJ (Fig. 5a). Over the western SOJ, the comma shaped WRF reflectivity band matches well with the observed cloud band accompanying MPV2. By 0600 UTC 4 February, WRF continues to compare well to the observed MPV1 cloud pattern and produces a band of locally high radar reflectivity that closely matches the observed cloud pattern along the JPCZ in the wake of the now dissipated MPV2 (Fig. 5b). The lowest half-η level winds also appear consistent with observed cloud streets. The close correspondence of the WRF reflectivity band to the observed cloud band along the JPCZ, including the arc-shaped structure and sinuous pattern near the Honshu coast, continues through the study period, although the simulated MPV1 low center is perhaps 200 km east of that inferred from satellite imagery (Figs. 5c,d).

Simulated soundings near the JPCZ at Matsue at 1200 UTC 3 and 4 February and at Wajima at 1200 UTC 5 February feature temperatures and dewpoints close to observed (Fig. 6). However, the stable layer at the top of the simulated boundary layer is lower and less defined than observed, biases that are common in WRF (e.g., Coniglio et al. 2013; Campbell et al. 2018). Winds near and beneath the inversion are generally within ~5 m s^{-1} and ~20° of observed. Overall, comparisons with *Himawari-8* imagery and the observed soundings indicate that WRF captures the mesoscale structure of the MPVs and JPCZ remarkably well, although boundary layer depths along the SOJ coast of Honshu are underdone. We now focus on the evolution of MPV2 and the formation of the JPCZ in its wake.

5. MPV2 and the development of the nascent JPCZ

Prior to the development of MPV2, locally warm air, low-level convergence, and weak troughing existed over the western SOJ near the base of the Korean Peninsula (Fig. 7a; troughing not explicitly shown). As cyclonic vorticity advection associated with the second upper-level short-wave trough moved over the SOJ (see also Fig. 3), convergence and associated troughing intensified, consistent with expectations from quasigeostrophic or potential vorticity theory and other MPV events over the SOJ (e.g., Montgomery and Farrell 1992; Yanase et al. 2002; Tsuboki and Asai 2004; Watanabe et al. 2018). Condensational warming within the accompanying cloud system and vortex stretching in the lee of the Korean Highlands likely aided low-level vorticity development (e.g., Nagata 1993). At 0000 UTC 3 February, the incipient MPV2 low center was at ~39.5°N, 129°E with northwesterly flow and cold advection to the southwest and south and cold advection in northeasterly flow to the northeast and north (Fig. 7b). By 0600 UTC 3 February, MPV2 developed a warm seclusion with a strong temperature gradient along a bent-back front rearward of the low center (Fig. 7c).

At this time, a band of heavy precipitation extended southward and southeastward along the developing JPCZ and bent-back front, wrapping partially around MPV2 and the precipitation-free warm seclusion (Fig. 8a). A cross section bisecting the warm seclusion (A–A′; cross sections here and elsewhere based on averages ±10 km normal to each cross section to reduce fine-scale variability and illustrate mesoscale structure) shows the strong temperature gradient, narrow plume of ascent, and precipitation band accompanying the bent-back front (Fig. 8b). This structure is similar to that found near the inner core of intense marine frontal

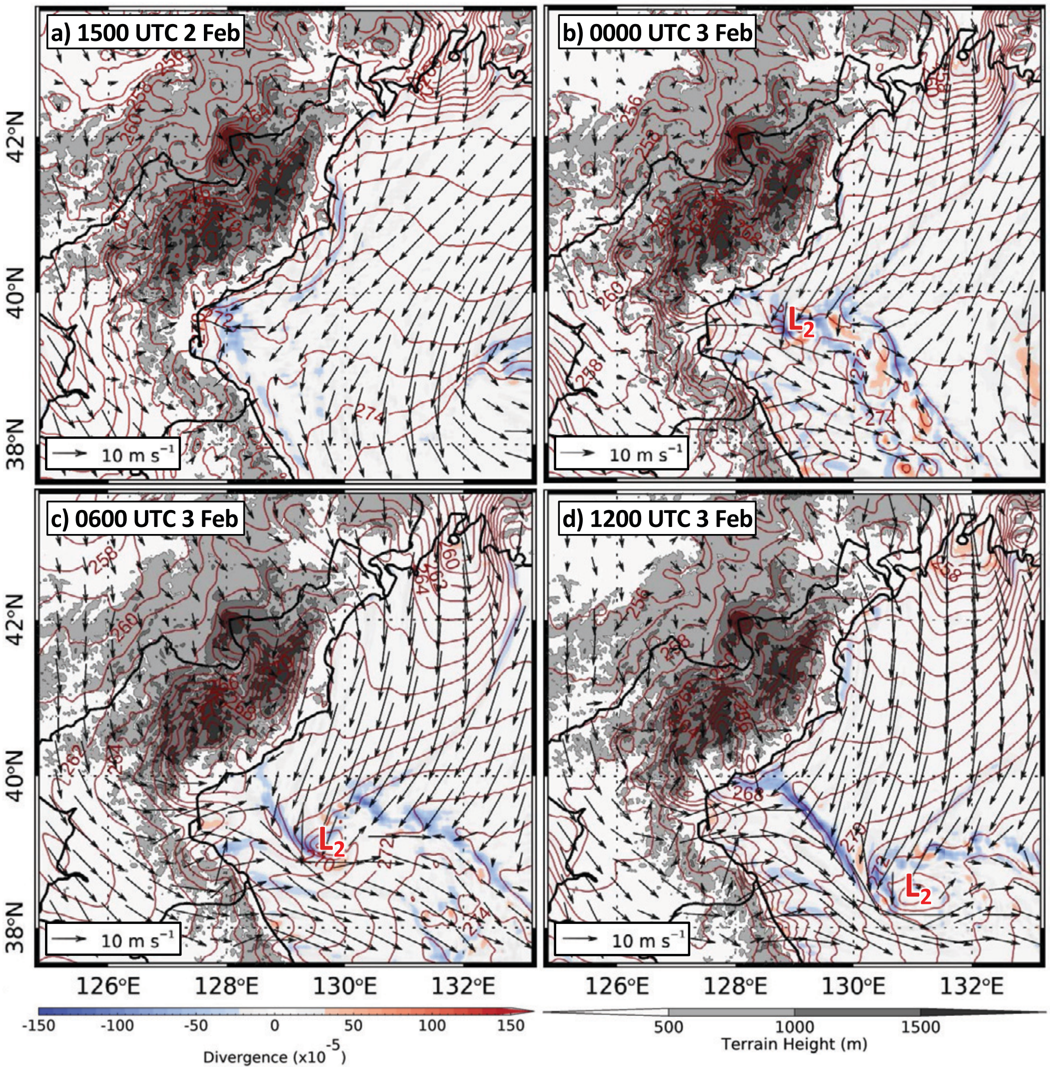

FIG. 7. WRF lowest half-η-level divergence (following the scale at bottom left), wind (vectors following the inset scale), potential temperature (red contours every 1 K), and terrain (following the scale at bottom right) at (a) 1500 UTC 2 Feb, (b) 0000 UTC 3 Feb, (c) 0600 UTC 3 Feb, and (d) 1200 UTC 3 Feb. MPV1 and MPV2 are identified with L1 and L2, respectively.

cyclones (e.g., Kuo et al. 1992; Neiman and Shapiro 1993). Three-dimensional trajectories ending at 0600 UTC 3 February on the lowest half-η level illustrate the airstreams and thermodynamic processes associated with the warm seclusion and bent-back front (Fig. 9a). The first airstream is composed of trajectories that originate over interior Asia, travel through the Khanka Lowlands of Russia, and terminate in the baroclinic zone north of the low center (maroon trajectories). The second airstream consists of trajectories that traverse the Korean Peninsula, move through the relatively low area between the Taebaek Mountains and Korean Highlands (the Taebaek Gap), and form the cold tongue that wraps equatorward and eastward around the low center (northernmost blue trajectories). A third airstream also traverses the Korean Peninsula but crosses the Taebaek Mountains instead of moving through the Taebaek Gap (southernmost blue trajectories).

The air within the warm seclusion has two different origins and is warmer because it experiences greater net thermodynamic modification than the surrounding air. To illustrate this, we focus on five trajectories ending within or around the warm seclusion (Fig. 9b). Trajectory 1 originates over interior Asia and travels through the Khanka Lowlands. It begins with the lowest potential temperature of the five trajectories (Fig. 9c) but ends in the center of the warm seclusion with the highest potential temperature since it experiences greater net warming from boundary layer and radiative processes over the SOJ (Fig. 9d) and, along with trajectory 4, the least diabatic cooling beneath precipitation features (Fig. 9e). Trajectory 5 began with the highest potential temperature but ends within the bent-back

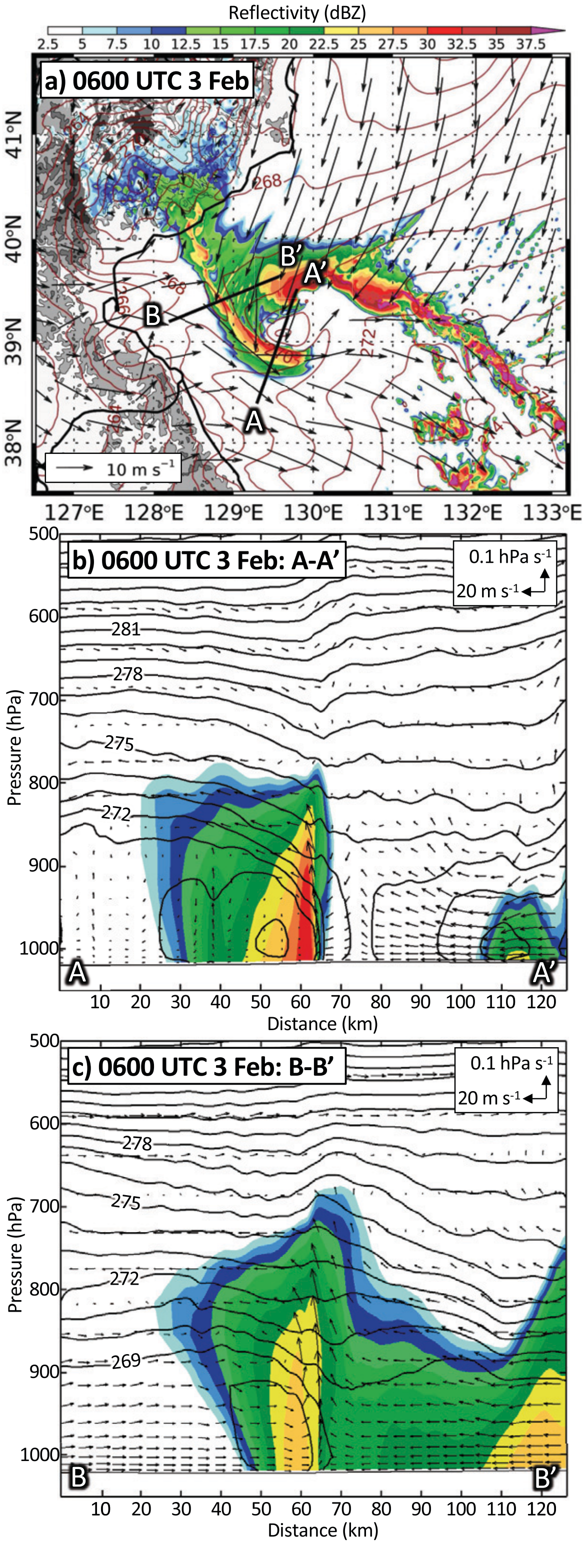

FIG. 8. (a) WRF lowest half-η-level radar reflectivity (following the scale at top), wind vectors (following the inset scale), potential temperature (red contours every 1 K), and terrain (as in Fig. 7) at 0600 UTC 3 Feb. (b) WRF cross section of radar reflectivity [using the scale in (a)], along-section circulation vectors (following the inset scale), and potential temperature (black contours every 1 K) along line A–A′ in (a). (c) As in (b), but along line B–B′.

front with the lowest potential temperature of the five trajectories since it experiences the least net warming from boundary layer and diabatic processes and, along with trajectories 2 and 3, the most diabatic cooling from precipitation.

Northwest of MPV2, cross section B–B′ illustrates the structure of the nascent JPCZ (Fig. 8c). At low levels, the JPCZ featured an enhanced potential temperature gradient exceeding 2 K (10 km)$^{-1}$ at which converging flow ascended in a narrow plume. Outflow aloft extended over the cooler air to the west but was weak to nonexistent to the east (temperature gradient not explicitly shown). Prior studies identify cross-JPCZ temperature contrasts (e.g., Yamaguchi and Magono 1974; Hozumi and Magono 1984) although, in contrast to the present case, Murakami (2019) found that six of seven JPCZ events examined by instrumented aircraft featured colder air to the north or east rather than to the southwest.

MPV2 continued its southeastward movement and by 1200 UTC was located at ~38.4°N, 131.0°E, with strong convergence along the lengthening JPCZ in its wake (Fig. 7d). Flow-parallel precipitation bands impinged from the northeast on the broader, more intense mesoscale precipitation band along the JPCZ (Fig. 10a). During this period, the JPCZ continued to feature a potential temperature gradient with colder air to the southwest. Cross section C–C′ taken across the JPCZ halfway between MPV2 and the Asian coast shows a similar pattern to that described previously (e.g., Fig. 8c) with convergent flow ascending in a narrow plume over the cross-JPCZ temperature gradient and outflow aloft strongest over the colder air to the southwest (Fig. 10b).

Trajectories ending on the lowest half-η level at 1200 UTC 3 February highlight the origins and evolution of four primary airstreams that terminate along the developing JPCZ (Fig. 11a). The first airstream terminates southwest of the JPCZ and features trajectories that move cyclonically around the western side of the Korean Highlands and channel through the Taeback Gap before spreading out over the SOJ (blue trajectories). The second airstream terminates northeast of the JPCZ and features trajectories that circumscribe the eastern side of the Korean Highlands and curve anticyclonically as they exit the Tumen Valley and environs (purple trajectories). The third airstream also terminates east of the JPCZ but travels from interior Asia through the Khanka Lowlands (brown trajectories). Fourth, a small number of trajectories move through a pass in the center of the Korean Highlands and end very near the Asian coast and upstream terminus of the JPCZ (green trajectories).

Thermodynamic histories along representative trajectories illustrate how differing airmass origins and thermodynamic modification over the SOJ contribute to the cross-JPCZ temperature gradient (Figs. 11b–d). Near MPV2, trajectory 6 begins northeast of the Korean Highlands with a higher initial

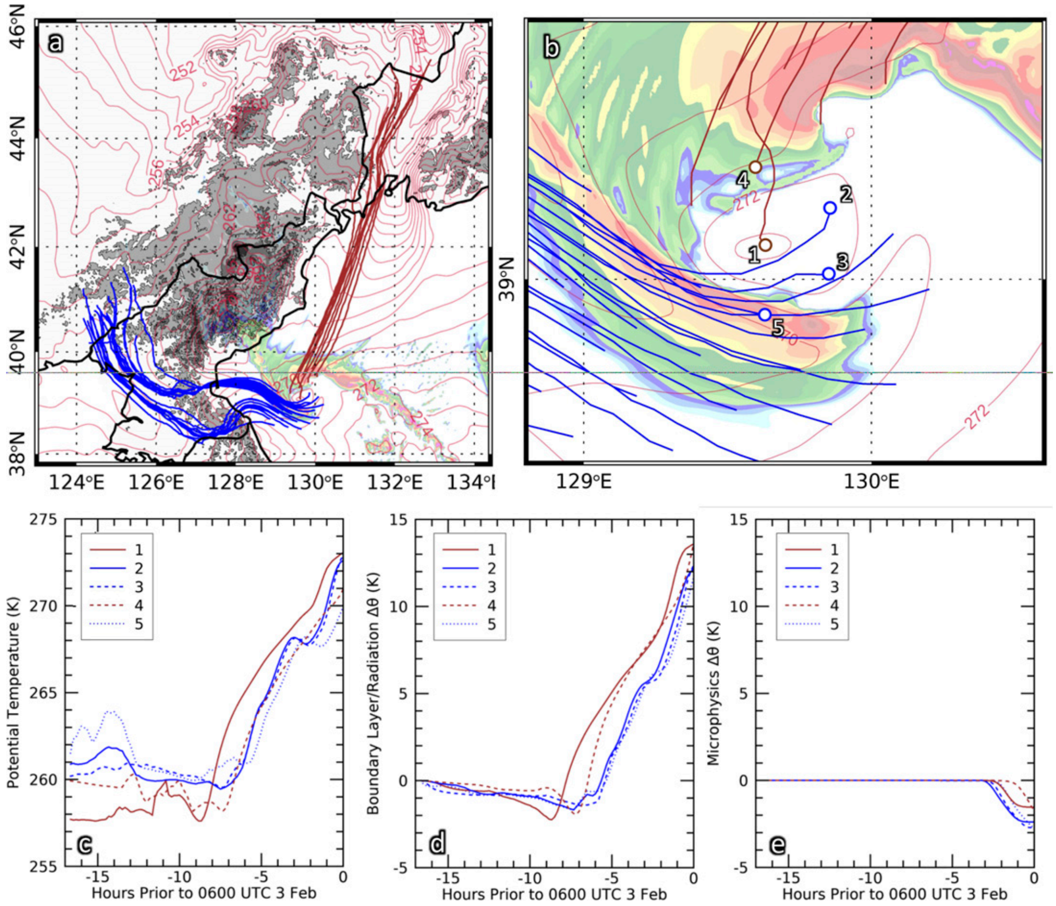

FIG. 9. (a) Three-dimensional, backward-calculated 17-h trajectories ending on the lowest half-η level at 0600 UTC 3 Feb. Trajectories are color coded as described in the text. Terrain color fill, reflectivity color fill, and potential temperature contours are as in Fig. 8a. (b) Close-up of the warm seclusion region with end points of selected trajectories annotated. (c) Potential temperature along selected trajectories identified in (b). (d) Potential temperature change along selected trajectories identified in (b) due to boundary layer and radiative diabatic processes. (e) As in (d), but due to microphysical diabatic processes.

potential temperature (~260 K) than trajectory 7 (Fig. 11b), which terminates on the warmer, northeast side of the JPCZ. However, trajectory 6 experiences a shorter fetch and less net heating due to boundary layer and radiative processes over the SOJ than trajectory 7 (Fig. 11c) and terminates on the southwest side of the JPCZ with a lower potential temperature. Diabatic cooling from precipitation along trajectories 6 and 7 is comparable and does not contribute to the cross-JPCZ temperature contrast (Fig. 11d). Farther north, trajectory 8 begins with a potential temperature that is about 1.5 K colder than trajectory 9 (Fig. 11b). It terminates with a potential temperature 2.5 K colder than trajectory 9, a result of less net warming from boundary layer and radiative processes (Fig. 11c). Thus, in this region, airmass origin and different thermodynamic histories contribute to the cross-JPCZ temperature contrast and the existence of colder air on the southwest side of the JPCZ.

In summary, the nascent JPCZ developed in the wake of MPV2, which formed in a region of a locally warm air, convergence, and troughing as cyclonic vorticity advection associated with an approaching 500-hPa trough moved over the SOJ. As it moved southeastward, MPV2 featured a warm seclusion and bent-back front. A trajectory ending in the center of the warm seclusion originated within colder air from Russia, but experienced greater net warming from boundary layer and radiative processes over the SOJ and less diabatic cooling beneath precipitation features. The bent-back front was structurally continuous with the nascent JPCZ, which lengthened as MPV2 moved southeastward. During this period the JPCZ featured three primary airstreams. The first moved cyclonically around the western side of the Korean Highlands and then eastward through Taeback Gap. The second and third moved through the Tumen Valley or the Khanka Lowlands, respectively, and then southwestward over the SOJ to the JPCZ. The cross-JPCZ temperature contrast with colder air to the southwest reflects the differing airmass origins and thermodynamic histories of these airstreams as they converged on the JPCZ.

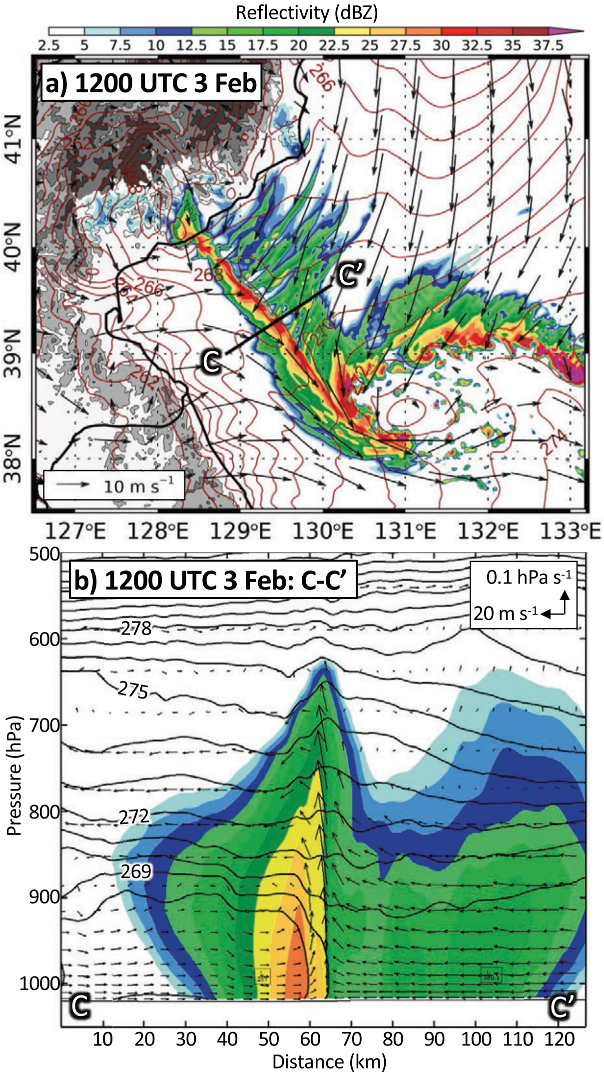

FIG. 10. As in Figs. 8a and 8b, but for 1200 UTC 3 Feb and (b) along line C–C′ in (a).

6. The mature JPCZ

By 0600 UTC 4 February, MPV2 had dissipated and the JPCZ extended across the western SOJ, becoming nearly parallel to the SOJ coast of Honshu near 36°N and intersecting the coast at ~36°N, 136°E (Fig. 12a). Relative to 1200 UTC 3 February, the cross-JPCZ temperature contrast was weaker and a broad warm tongue (i.e., an axis of maximum temperature) was nearly collocated with the JPCZ, which was flanked on both sides by cold advection (cf. Figs. 7d and 12a). This general pattern predominated through 0600 UTC 5 February (Fig. 12b). The JPCZ finally dissipated on 7 February (not shown).

Model-derived reflectivity at 0600 UTC 5 February showed that the mature JPCZ featured wind-parallel bands and other convective cells on its northeast flank (near the Asian coast) and northern flank (near Honshu) that merged into the broader, quasi-continuous precipitation band along the JPCZ (Fig. 13a). Careful inspection of the potential temperature analysis reveals that the axis of warmest temperature associated with the warm tongue was located just northeast of the JPCZ near the Asian coast but shifted to south of the JPCZ near Honshu. This shift reflects a reversal of the cross-JPCZ temperature gradient from the Asian coast to Honshu with the coldest air southwest of the JPCZ near the former and north of the JPCZ near the latter. The precipitation band along the JPCZ broadened and developed wavelike features that grew in scale as they approached Honshu. A near-surface relative-vorticity analysis at this time illustrates the strengthening and upscale growth of cyclonic vortical disturbances along the JPCZ (Fig. 14), as identified in other JPCZ events and attributed to horizontal shear instability (e.g., Nagata 1993; Kawashima and Fujiyoshi 2005).

Three cross sections at 0600 UTC 5 February illustrate changes in the structure of the mature JPCZ from the Asian coast to Honshu (Figs. 13b–d). Near the Asian coast, cross section D–D′ shows a similar structure to that described earlier in this region with convergent flow ascending in a narrow plume at the cross-JPCZ temperature gradient (Fig. 13b). Colder air still exists to the southwest of the JPCZ, but the temperature gradient has weakened relative to 1200 UTC 3 February and the outflow is now more symmetrical with an "in, up, and out" secondary circulation, although the outflow is stronger and more elevated on the northeast side of the JPCZ (cf. Figs. 10b and 13b). Farther southeast, the cross-JPCZ temperature gradient in cross section E–E′ was much weaker, the JPCZ was roughly collocated with the warm tongue. and the vertical motion was weaker and broader (Fig. 13c). The latter is consistent with the broader precipitation band and the presence of multiple embedded convective features.

Near the coast of Honshu, the warm tongue in cross section F–F′ was south of the JPCZ, with the coldest air north of the JPCZ (Fig. 13d). In this region, the precipitation pattern and cross-JPCZ secondary circulation varied in structure and strength due to the influence of the cyclonic vortical features. Along cross section F–F′, a narrow plume of shallow ascent existed at the JPCZ, with broad ascent aloft to the north above the colder northerly flow at low levels. Outflow was strongest on the north side of the JPCZ, and scattered precipitation cells existed in the warm tongue to the south. In summary, these three cross sections illustrate a reversal in the cross-JPCZ temperature gradient and structure and strength of the cross-JPCZ secondary circulation from the Asian coast to Honshu.

Trajectories ending on the lowest-half-η level at 0600 UTC 5 February continued to depict the mature JPCZ as a prominent airstream boundary (Fig. 15a). Trajectories ending southwest or south of the JPCZ move cyclonically around the Korean Highlands or travel from China over the Yellow Sea before traversing the Korean Peninsula and Taebaek Mountains (blue trajectories; Fig. 15a). In contrast to trajectories ending at 1200 UTC 3 February, there is less flow channeling of these trajectories through Taebaek gap, although they

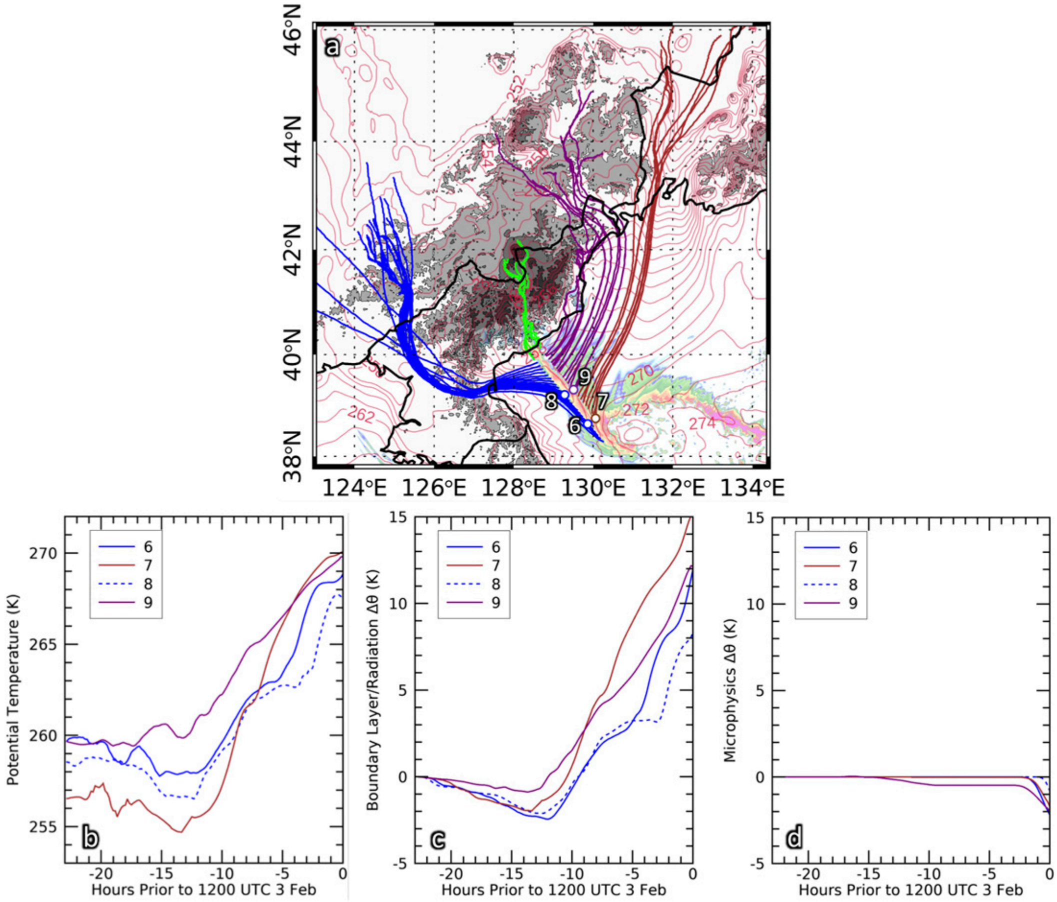

FIG. 11. (a) Three-dimensional, backward-calculated 23-h trajectories ending on the lowest half-η level at 1200 UTC 3 Feb. Trajectories are color coded as described in the text. Terrain color fill, reflectivity color fill, and potential temperature contours are as in Fig. 8a. (b) Potential temperature along selected trajectories identified in (a). (c) Potential temperature change along selected trajectories identified in (a) due to boundary layer and radiative diabatic processes. (d) As in (c), but due to microphysical diabatic processes.

continue to traverse the Taebaek Mountains (cf. Figs. 11a and 15a). Trajectories ending northeast or north of the JPCZ either circumscribe the eastern side of the Korean Highlands, moving over the SOJ from the Tumen Valley and environs (purple trajectories; Fig. 15a) or travel from interior Asia through the Khanka Lowlands (maroon trajectories; Fig. 15a), fanning out over the SOJ.

Thermodynamic histories for selected trajectory pairs across the JPCZ show how airmass origin and modification over the SOJ affect the cross-JPCZ temperature gradient (Figs. 15b–d). Near the Asian coast, trajectory 10, which terminates on the colder, southwest side of the JPCZ, circumscribes the western side of the Korean Highlands, cools slowly while over land, and then warms dramatically after moving over the SOJ (Figs. 15b,c). In contrast, trajectory 11, which terminates opposite trajectory 10 on the warmer, northeast side of the JPCZ, begins with a much lower potential temperature and similarly cools over land, but has a longer fetch over the SOJ and experiences greater thermodynamic modification, ending with a higher potential temperature than trajectory 10. Thus, near the coast of Asia, the shorter over-SOJ fetch and reduced thermodynamic modification of trajectories emerging from the Korean Peninsula yield colder air to the southwest of the SOJ despite this air mass being initially warmer upstream than the air emerging from the Tumen Valley and environs. Farther southeast, the large initial potential temperature contrast between trajectories 12 and 13 is nearly perfectly balanced by differences in fetch and thermodynamic modification over the SOJ (cf. Figs. 15b and 15c), so that the two trajectories impinge on the JPCZ with nearly identical potential temperatures, resulting in a warm tongue. Near the coast of Honshu, trajectory 14 not only begins with a higher potential temperature than trajectory 15 (Fig. 15b) but, because of its long residence time over the relatively warm waters of the southern SOJ, also experiences substantial thermodynamic modification (Fig. 15c). Ultimately, it impinges on the JPCZ with a higher potential temperature than trajectory 15, so that the coldest air in this region is north of the JPCZ. Along all of these trajectories, the magnitude of diabatic heating or cooling from precipitation is ≤ 1.5 K (Fig. 15d).

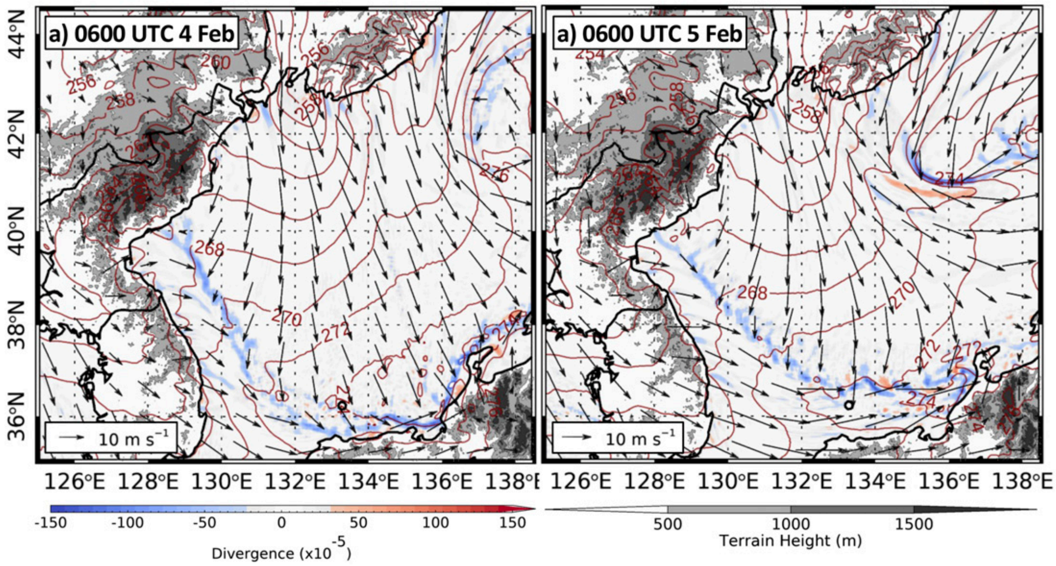

FIG. 12. WRF lowest half-η-level divergence (following the color scale at bottom left), wind (vectors following the inset scale), potential temperature (red contours every 2 K), and terrain (following the scale at bottom right) at (a) 0600 UTC 4 Feb and (b) 0600 UTC 5 Feb.

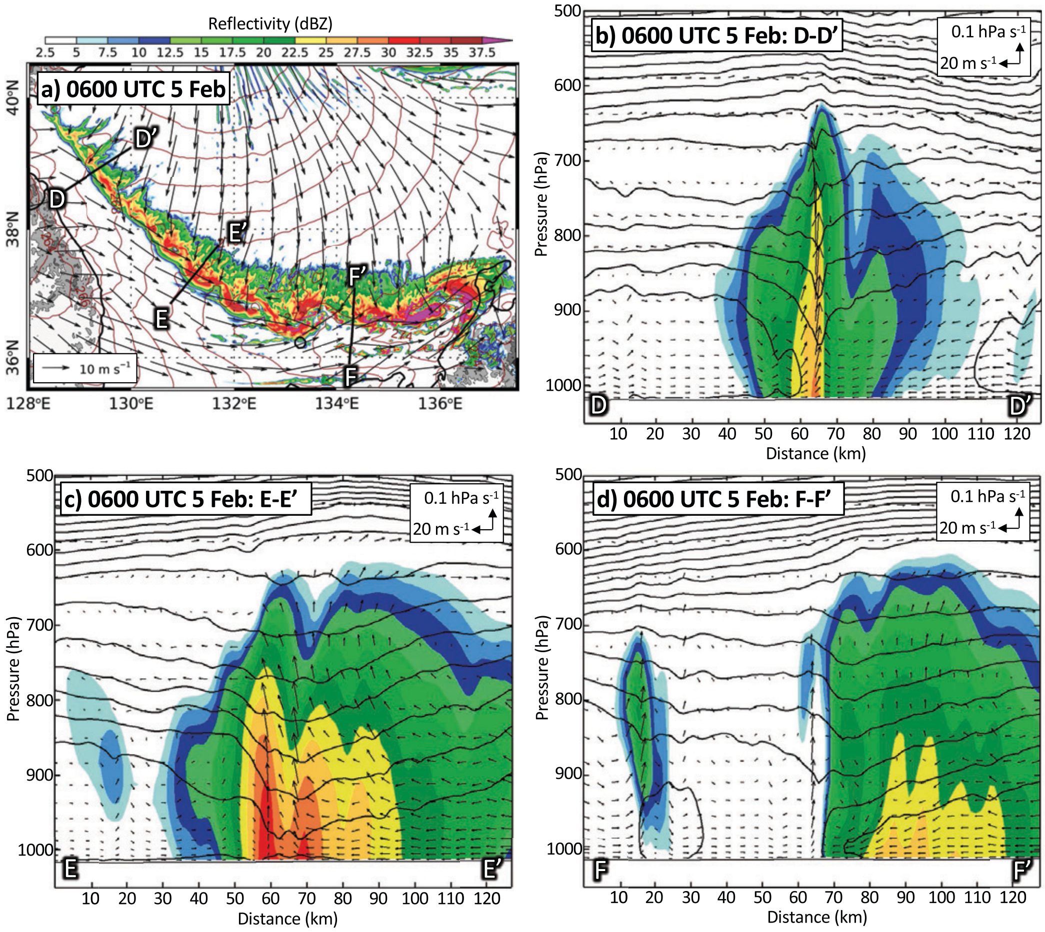

FIG. 13. As in Fig. 8, but for 0600 UTC 5 Feb and (b) along line D–D′ in (a), (c) along line E–E′ in (a), and (d) along line F–F′ in (a).

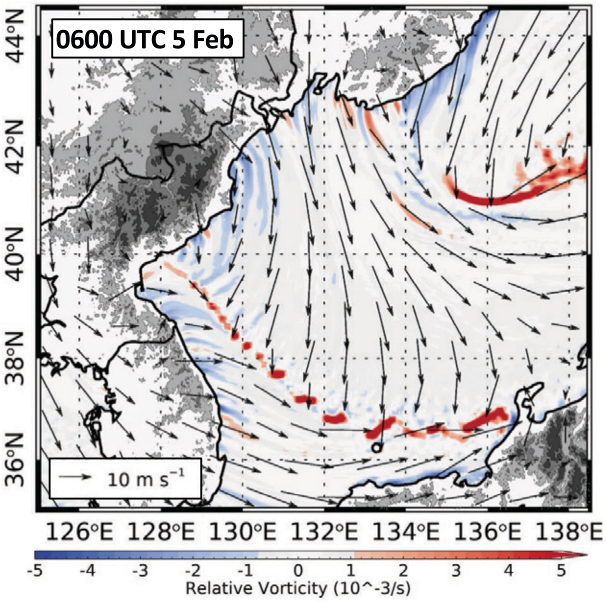

FIG. 14. WRF lowest half-η-level relative vorticity (following the color scale at bottom), lowest-level wind (vectors following the inset scale) and terrain (as in Fig. 7) at 0600 UTC 5 Feb.

Collectively, these trajectories highlight how flow interaction with the Korean Highlands, cold-air pathways from interior Asia, and airmass modification over the SOJ affect the thermodynamic structure of the mature JPCZ. Flow splitting occurs upstream of the Korean Highlands, resulting in two major airstreams that converge into the JPCZ downstream of the base of the Korean Peninsula. The airstream circumscribing the west side of the Korean Highlands and traversing the Korean Peninsula is potentially warmer upstream over Asia than the airstream to the east that emerges from the Tumen Valley. Near the coast of Asia, however, the airstream emerging from the Korean Peninsula has a shorter fetch over the SOJ relative to that emerging from the Tumen Valley, leading to colder air to the southwest of the JPCZ. In contrast, near Honshu, the JPCZ separates airstreams emerging from the Korean Peninsula and the Khanka Lowlands. Both airstreams have substantial over-SOJ fetches, the former over the relatively warm waters of the southwest SOJ. Ultimately, this leads to a reversal of the cross-JPCZ temperature gradient with colder air to the north near Honshu. Thus, the cross-JPCZ reverses due to differing origins, over SOJ fetch, and thermodynamic histories of airstreams impinging on the JPCZ.

7. Conclusions

Using *Himawari-8* imagery, the ERA5 reanalysis, and WRF simulations, this paper has examined the formation, thermodynamic structure, and airflows of a Japan Sea polar-airmass convergence zone that formed in the wake of a mesoscale polar vortex (labeled MPV2) during a cold-air outbreak (CAO) from 2 to 7 February 2018. MPV2 formed within a region of locally warm air, low-level convergence, and weak troughing as an upper-level trough moved downstream of the Korean Highlands and over the Sea of Japan (SOJ) on 3 February. Although small in scale, MPV2 developed a warm seclusion and bent-back front similar to that observed in intense marine cyclones (e.g., Kuo et al. 1992; Neiman and Shapiro 1993). The warm seclusion consisted of air that moved over the SOJ that moved through the Taebaek gap of Korea and the Khanka Lowlands of Russia, with the warmth of air in the seclusion reflecting greater net thermodynamic modification over the SOJ relative to the surrounding air mass.

The nascent JPCZ was structurally continuous with the bent-back front and lengthened as MPV2 moved southeastward. Eventually, MPV2 dissipated and the mature JPCZ extended across the SOJ to Honshu. Wind-parallel and other precipitation features converged into the broader, mesoscale precipitation band along the JPCZ from the northeast. The mesoscale precipitation band broadened and developed wavelike features as it approached Honshu due to strengthening and growth of cyclonic vortical disturbances, as observed in other JPCZ events (e.g., Nagata 1993; Kawashima and Fujiyoshi 2005).

The thermodynamic structure of the mature JPCZ varied from the Asian to the Honshu coast. Near Asia, the JPCZ featured a low-level temperature gradient with colder air to the southwest and a narrow plume of ascent. As the JPCZ approached Honshu, the low-level temperature gradient weakened and eventually reversed, with the colder air to the north. Additionally, the precipitation pattern and cross-JPCZ secondary circulation varied in structure and strength, especially near Honshu due to the influence of the vortical disturbances.

The reversal of the cross-JPCZ temperature gradient along the mature JPCZ reflected both the origins and thermodynamic histories of airflows converging on the JPCZ, as suggested by Yamaguchi and Magono (1974) and Hozumi and Magono (1984). Trajectories emerging from the Korean Peninsula and terminating to the southwest or south of the JPCZ begin over continental Asia with potential temperatures comparable to or warmer than trajectories emerging from the Tumen Valley or Khanka Lowlands that terminate to the northeast or north of the JPCZ. However, near the coast of Asia, trajectories emerging from the Korean Peninsula have a shorter over-SOJ fetch and experience less thermodynamic modification, yielding colder air to the southwest of the JPCZ. Near Honshu, trajectories emerging from the Korean Peninsula have a sufficiently long residence time over the relatively warm waters of the southwest SOJ that this airstream is warmer than that impinging on the JPCZ from the north, resulting in a reversal of the cross-JPCZ temperature gradient near Honshu.

As summarized by Murakami (2019), the thermal structure of the JPCZ is a point of controversy in the literature. We propose that the cross-JPCZ temperature gradient may vary spatially and temporally due to the differing characteristics, origins, and thermodynamic histories of airstreams impinging on the JPCZ. It is possible that near Honshu, these characteristics, origins, and thermodynamic histories favor colder air to the north of the JPCZ, which may help explain why six of

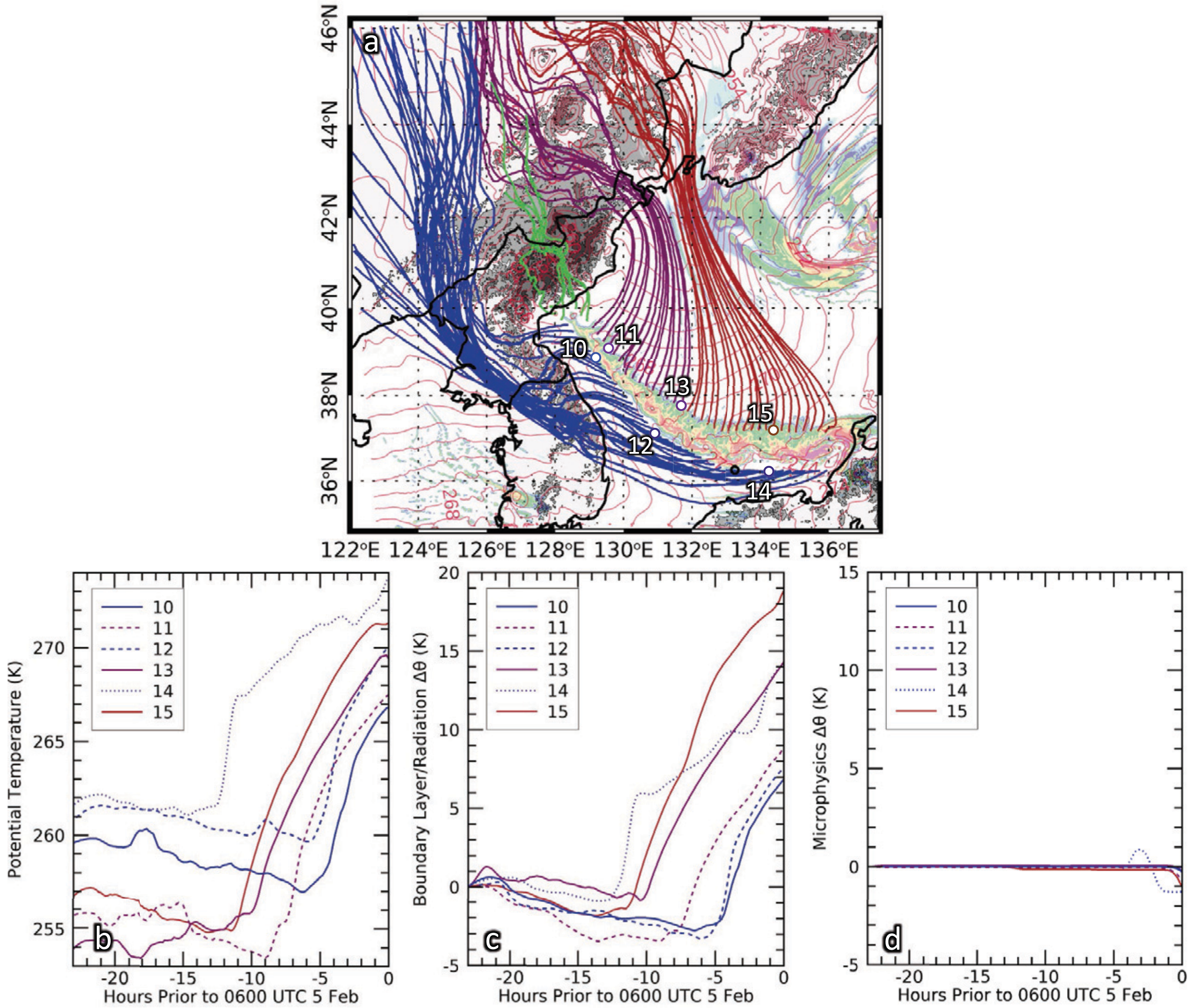

FIG. 15. (a) Three-dimensional, backward-calculated 48-h trajectories ending on the lowest half-η level at 0600 UTC 5 Feb. Trajectories are color coded as described in the text. Terrain color fill, reflectivity color fill, and potential temperature contours are as in Fig. 8a. (b) Potential temperature along selected trajectories identified in (a) for the last 23 h of the trajectory integration. (c) Potential temperature change along selected trajectories identified in (a) for the last 23 h of the trajectory integration due to boundary layer and radiative diabatic processes. (d) As in (c), but due to microphysical diabatic processes.

seven JPCZ events examined by instrumented aircraft and summarized by Murakami (2019) featured colder air to the north rather than to the south. Such a hypothesis could be explored in future work using high-resolution reanalyses or regional climate simulations such as those used by Shinoda et al. (2021) to examine the influence of the Korean Highlands and Korean Peninsula on the formation and maintenance of the JPCZ. Also of interest for future work is how these airflows and thermodynamic structures affect distribution and intensity of precipitation, especially snowfall, along the Honshu coast and adjoining topography.

Acknowledgments. This research is based in part on work supported by National Science Foundation Grants AGS-1635654 and AGS-1929602. The first author was supported by the U.S. Air Force Institute of Technology (AFIT) and recognizes AFIT's key role in this work. Any opinions, findings, and conclusions expressed in this article are those of the authors and do not necessarily reflect the policy, position, or views of the National Science Foundation, U.S. government, U.S. Department of Defense, or U.S. Air Force. The WRF Model, computation time on the Cheyenne supercomputer (https://doi.org/10.5065/D6RX99HX), and GFS model data from the Research Data Archive (https://doi.org/10.5065/D65D8PWK; https://rda.ucar.edu/datasets/ds084.1/) were provided by the National Center for Atmospheric Research, sponsored by the National Science Foundation. Computer support was also provided by the University of

Utah Center for High Performance Computing. Insightful comments from Jay Mace, Steve Krueger, Gannet Hallar, Jeremy Gibbs, Peter Veals, Tom Gowan, and Leah Campbell greatly enhanced this work.

Data availability statement. Contact the corresponding author for access to the WRF Model output, which is stored on servers at the University of Utah Center for High Performance Computing. Other datasets are available as described in the paper.

REFERENCES

Alcott, T. I., and W. J. Steenburgh, 2013: Orographic influences on a Great Salt Lake–effect snowstorm. *Mon. Wea. Rev.*, **141**, 2432–2450, https://doi.org/10.1175/MWR-D-12-00328.1.

——, ——, and N. F. Laird, 2012: Great Salt Lake–effect precipitation: Observed frequency, characteristics, and environmental factors. *Wea. Forecasting*, **27**, 954–971, https://doi.org/10.1175/WAF-D-12-00016.1.

Andersson, T., and S. Nilsson, 1990: Topographically inducted convective snowbands over the Baltic Sea and their precipitation distribution. *Wea. Forecasting*, **5**, 299–312, https://doi.org/10.1175/1520-0434(1990)005<0299:TICSOT>2.0.CO;2.

——, and N. Gustafsson, 1994: Coast of departure and coast of arrival: Two important concepts for the formation and structure of convective snowbands over seas and lakes. *Mon. Wea. Rev.*, **122**, 1036–1049, https://doi.org/10.1175/1520-0493(1994)122<1036:CODACO>2.0.CO;2.

Asai, T., 1988: Meso-scale features of heavy snowfalls in Japan Sea coastal regions of Japan (in Japanese). *Tenki*, **35**, 156–161.

Bergmaier, P. T., B. Geerts, L. S. Campbell, and W. J. Steenburgh, 2017: The OWLeS IOP2b lake-effect snowstorm: Dynamics of the secondary circulation. *Mon. Wea. Rev.*, **145**, 2437–2459, https://doi.org/10.1175/MWR-D-16-0462.1.

Businger, S., and B. Walter, 1988: Comma cloud development and associated rapid cyclogenesis over the Gulf of Alaska: A case study using aircraft and operational data. *Mon. Wea. Rev.*, **116**, 1103–1123, https://doi.org/10.1175/1520-0493(1988)116<1103:CCDAAR>2.0.CO;2.

Campbell, L. S., and W. J. Steenburgh, 2017: The OWLeS IOP2b lake-effect snowstorm: Mechanisms contributing to the Tug Hill precipitation maximum. *Mon. Wea. Rev.*, **145**, 2461–2478, https://doi.org/10.1175/MWR-D-16-0461.1.

——, ——, Y. Yamada, M. Kawashima, and Y. Fujiyoshi, 2018: Influences of orography and coastal geometry on a transverse-mode sea-effect snowstorm over Hokkaido Island, Japan. *Mon. Wea. Rev.*, **146**, 2201–2220, https://doi.org/10.1175/MWR-D-17-0286.1.

Chen, F., and J. Dudhia, 2001: Coupling an advanced land surface–hydrology model with the Penn State–NCAR MM5 modeling system. Part II: Preliminary model validation. *Mon. Wea. Rev.*, **129**, 587–604, https://doi.org/10.1175/1520-0493(2001)129<0587:CAALSH>2.0.CO;2.

Coniglio, M. C., J. Correia, P. T. Marsh, and F. Kong, 2013: Verification of convection-allowing WRF Model forecasts of the planetary boundary layer using sounding observations. *Wea. Forecasting*, **28**, 842–862, https://doi.org/10.1175/WAF-D-12-00103.1.

Copernicus Climate Change Service, 2017: ERA5: Fifth generation of ECMWF atmospheric reanalyses of the global climate. Copernicus Climate Change Service (C3S) Climate Data Store (CDS). Accessed 20 March 2019, https://cds.climate.copernicus.eu/cdsapp#!/dataset/reanalysis-era5-single-levels?tab=overview; https://cds.climate.copernicus.eu/cdsapp#!/dataset/reanalysis-era5-pressure-levels?tab=overview.

Dorman, C. E., and Coauthors, 2004: Winter marine atmospheric conditions over the Japan Sea. *J. Geophys. Res.*, **109**, C12011, https://doi.org/10.1029/2001JC001197.

Dudhia, J., 1989: Numerical study of convection observed during the Winter Monsoon Experiment using a mesoscale two-dimensional model. *J. Atmos. Sci.*, **46**, 3077–3107, https://doi.org/10.1175/1520-0469(1989)046<3077:NSOCOD>2.0.CO;2.

Eito, H., T. Kato, M. Yoshizaki, and A. Adachi, 2005: Numerical simulation of the quasi-stationary snowband observed over the southern coastal area of the Sea of Japan on 16 January 2001. *J. Meteor. Soc. Japan*, **83**, 551–576, https://doi.org/10.2151/jmsj.83.551.

——, M. Murakami, C. Muroi, T. Kato, S. Hayashi, and H. Kuroiwa, 2010: The structure and formation mechanism of transversal cloud bands associated with the Japan-Sea polar-air-mass convergence zone. *J. Meteor. Soc. Japan*, **88**, 625–648, https://doi.org/10.2151/jmsj.2010-402.

Endoh, T., K. Hozumi, and C. Magono, 1984: Formation mechanism of a notable cloud system that causes heavy snowfall and a tentative prediction of its behavior. *Natl. Disaster Sci.*, **6**, 31–42.

Estoque, M. A., and K. Ninomiya, 1976: Numerical simulation of Japan Sea effect snowfall. *Tellus*, **28**, 243–253, https://doi.org/10.3402/tellusa.v28i3.10285.

Føre, I., J. E. Kristjánsson, E. W. Kolstad, T. J. Bracegirdle, Ø. Saetra, and B. Røsting, 2012: A 'hurricane-like' polar low fueled by sensible heat flux: High-resolution numerical simulations. *Quart. J. Roy. Meteor. Soc.*, **138**, 1308–1324, https://doi.org/10.1002/qj.1876.

Fu, G., H. Niino, R. Kimura, and T. Kato, 2004: A polar low over the Japan Sea on 21 January 1997. Part I: Observational analysis. *Mon. Wea. Rev.*, **132**, 1537–1551, https://doi.org/10.1175/1520-0493(2004)132<1537:APLOTJ>2.0.CO;2.

Gowan, T. M., 2019: Trajectories. Personal GitHub page, accessed 9 October 2019, https://github.com/tomgowan/trajectories.

Hersbach, H., and Coauthors, 2020: The ERA5 global reanalysis. *Quart. J. Roy. Meteor. Soc.*, **146**, 1999–2049, https://doi.org/10.1002/qj.3803.

Higuchi, K., 1963: The band structure of snowfalls. *J. Meteor. Soc. Japan*, **41**, 53–70, https://doi.org/10.2151/jmsj1923.41.1_53.

Hong, S.-Y., Y. Noh, and J. Dudhia, 2006: A new vertical diffusion package with an explicit treatment of entrainment processes. *Mon. Wea. Rev.*, **134**, 2318–2341, https://doi.org/10.1175/MWR3199.1.

Hozumi, K., and C. Magono, 1984: The cloud structure of convergent cloud bands over the Japan Sea in winter monsoon period. *J. Meteor. Soc. Japan*, **62**, 522–533, https://doi.org/10.2151/jmsj1965.62.3_522.

Iacono, M. J., J. S. Delamere, E. J. Mlawer, M. W. Shephard, S. A. Clough, and W. D. Collins, 2008: Radiative forcing by long-lived greenhouse gases: Calculations with the AER radiative transfer models. *J. Geophys. Res.*, **113**, D13103, https://doi.org/10.1029/2008JD009944.

Jiménez, P. A., J. Dudhia, J. F. González-Rouco, J. Navarro, J. P. Montávez, and E. García-Bustamante, 2012: A revised scheme for the WRF surface layer formulation. *Mon. Wea. Rev.*, **140**, 898–918, https://doi.org/10.1175/MWR-D-11-00056.1.

Kain, J. S., 2004: The Kain–Fritsch convective parameterization: An update. *J. Appl. Meteor.*, **43**, 170–181, https://doi.org/10.1175/1520-0450(2004)043<0170:TKCPAU>2.0.CO;2.

Kawamoto, T. S., S. Miyazawa, and K. Fuj, 1963: Heavy snowfalls caused by the Hokuriku Front (in Japanese). *Kishokenkyu Note*, **14**, 56–70.

Kawashima, M., and Y. Fujiyoshi, 2005: Shear instability wave along a snowband: Instability structure, evolution, and energetics derived from dual-Doppler radar data. *J. Atmos. Sci.*, **62**, 351–370, https://doi.org/10.1175/JAS-3392.1.

Kindap, T., 2010: A severe sea-effect snow episode over the city of Istanbul. *Nat. Hazards*, **54**, 707–723, https://doi.org/10.1007/s11069-009-9496-7.

Kristovich, D. A. R., and Coauthors, 2017: The Ontario Winter Lake-effect Systems (OWLeS) field campaign: Scientific and educational adventures to further our knowledge and prediction of lake-effect storms. *Bull. Amer. Meteor. Soc.*, **98**, 315–332, https://doi.org/10.1175/BAMS-D-15-00034.1.

Kuo, Y.-H., R. J. Reed, and S. Low-Nam, 1992: Thermal structure and airflow in a model simulation of an occluded marine cyclone. *Mon. Wea. Rev.*, **120**, 2280–2297, https://doi.org/10.1175/1520-0493(1992)120<2280:TSAAIA>2.0.CO;2.

Kusunoki, K., M. Murakami, N. Orikasa, M. Hoshimoto, and Y. Tanaka, 2005: Observations of quasi-stationary and shallow orographic snow clouds: Spatial distributions of supercooled liquid water and snow particles. *Mon. Wea. Rev.*, **133**, 743–751, https://doi.org/10.1175/MWR2874.1.

Kyodo News, 2018: Gallery: Heavy snow in central Japan. Accessed 7 September 2021, https://english.kyodonews.net/news/2018/02/b399959683d7-gallery-heavy-snow-in-central-japan.html.

Laird, N. F., D. A. R. Kristovich, and J. E. Walsh, 2003: Idealized model simulations examining the mesoscale structure of winter lake-effect circulations. *Mon. Wea. Rev.*, **131**, 206–221, https://doi.org/10.1175/1520-0493(2003)131<0206:IMSETM>2.0.CO;2.

——, J. Desrochers, and M. Payer, 2009: Climatology of lake-effect precipitation events over Lake Champlain. *J. Appl. Meteor. Climatol*, **48**, 232–250, https://doi.org/10.1175/2008JAMC1923.1.

Magono, C., 1971: On the localization phenomena of snowfall. *J. Meteor. Soc. Japan*, **49**, 824–835, https://doi.org/10.2151/jmsj1965.49A.0_824.

——, K. Kikuchi, T. Kimura, S. Tazawa, and T. Kasai, 1966: A study on the snowfall in the winter monsoon season in Hokkaido with special reference to low land snowfall. *J. Fac. Sci. Hokkaido Univ. Ser.*, **11**, 287–308.

McMillen, J. D., and W. J. Steenburgh, 2015a: Impact of microphysics parameterizations on simulations of the 27 October 2010 Great Salt Lake effect snowstorm. *Wea. Forecasting*, **30**, 136–152, https://doi.org/10.1175/WAF-D-14-00060.1.

——, and ——, 2015b: Capabilities and limitations of convection-permitting WRF simulations of lake-effect systems over the Great Salt Lake. *Wea. Forecasting*, **30**, 1711–1731, https://doi.org/10.1175/WAF-D-15-0017.1.

Miltenberger, A. K., S. Pfahl, and H. Wernli, 2013: An online trajectory module (version 1.0) for the nonhydrostatic numerical weather prediction model COSMO. *Geosci. Model Dev.*, **6**, 1989–2004, https://doi.org/10.5194/gmd-6-1989-2013.

Mitnik, L. M., 1992: Mesoscale coherent structures in the surface wind field during cold air outbreaks over the Far Eastern seas from the satellite side looking radar. *La Mer*, **30**, 287–296.

Montgomery, M. T., and B. F. Farrell, 1992: Polar low dynamics. *J. Atmos. Sci.*, **49**, 2484–2505, https://doi.org/10.1175/1520-0469(1992)049<2484:PLD>2.0.CO;2.

Murakami, M., 2019: Inner structures of snow clouds over the Sea of Japan observed by instrumented aircraft: A review. *J. Meteor. Soc. Japan*, **97**, 5–38, https://doi.org/10.2151/jmsj.2019-009.

Nagata, M., 1987: On the structure of a convergent cloud band over the Japan Sea in winter; a prediction experiment. *J. Meteor. Soc. Japan*, **65**, 871–883, https://doi.org/10.2151/jmsj1965.65.6_871.

——, 1991: Further numerical study on the formation of the convergent cloud band over the Japan Sea in winter. *J. Meteor. Soc. Japan*, **69**, 419–428, https://doi.org/10.2151/jmsj1965.69.3_419.

——, 1992: Modeling case study of the Japan-Sea convergent cloud band in a varying large-scale environment. *J. Meteor. Soc. Japan*, **70**, 649–671, https://doi.org/10.2151/jmsj1965.70.1B_649.

——, 1993: Meso-β-scale vortices developing along the Japan-Sea polar-airmass convergence zone (JPCZ) cloud band: Numerical simulation. *J. Meteor. Soc. Japan*, **71**, 43–57, https://doi.org/10.2151/jmsj1965.71.1_43.

——, M. Ikawa, S. Yoshizumi, and T. Yoshida, 1986: On the formation of a convergent cloud band over the Japan Sea in winter; numerical experiments. *J. Meteor. Soc. Japan*, **64**, 841–855, https://doi.org/10.2151/jmsj1965.64.6_841.

Nakai, S., and T. Endoh, 1995: Observation of snowfall and airflow over a low mountain barrier. *J. Meteor. Soc. Japan*, **73**, 183–199, https://doi.org/10.2151/jmsj1965.73.2_183.

——, K. Iwanami, R. Misumi, S. G. Park, and T. Kobayashi, 2005: A classification of snow clouds by Doppler radar observations at Nagaoka, Japan. *SOLA*, **1**, 161–164, https://doi.org/10.2151/sola.2005-042.

——, and Coauthors, 2012: A Snow Disaster Forecasting System (SDFS) constructed from field observations and laboratory experiments. *Cold Reg. Sci. Technol.*, **70**, 53–61, https://doi.org/10.1016/j.coldregions.2011.09.002.

NCEP, 2015: NCEP GFS 0.25 degree global forecast grids historical archive. Dept. of Commerce/NOAA/NWS/NCEP, Research Data Archive at the National Center for Atmospheric Research Computational and Information Systems Laboratory, accessed 15 August 2018, https://doi.org/10.5065/D65D8PWK.

Neiman, P. J., and M. A. Shapiro, 1993: The life cycle of an extratropical marine cyclone. Part I: Frontal-cyclone evolution and thermodynamic air–sea interaction. *Mon. Wea. Rev.*, **121**, 2153–2176, https://doi.org/10.1175/1520-0493(1993)121<2153:TLCOAE>2.0.CO;2.

Ninomiya, K., 1989: Polar/comma-cloud lows over the Japan Sea and the northwestern Pacific in winter. *J. Meteor. Soc. Japan*, **67**, 83–97, https://doi.org/10.2151/jmsj1965.67.1_83.

Niziol, T. A., W. R. Snyder, and J. S. Waldstreicher, 1995: Winter weather forecasting throughout the eastern United States. Part IV: Lake effect snow. *Wea. Forecasting*, **10**, 61–77, https://doi.org/10.1175/1520-0434(1995)010<0061:WWFTTE>2.0.CO;2.

Norris, J., G. Vaughan, and D. M. Schultz, 2013: Snowbands over the English Channel and Irish Sea during cold-air outbreaks. *Quart. J. Roy. Meteor. Soc.*, **139**, 1747–1761, https://doi.org/10.1002/qj.2079.

Ogura, Y., 1991: Vortex over the Sea of Japan in winter (in Japanese). *Kisho*, **35**, 32–34.

Ohigashi, T., and K. Tsuboki, 2007: Shift and intensification processes of the Japan-Sea polar-airmass convergence zone associated with the passage of a mid-tropospheric cold core. *J. Meteor. Soc. Japan*, **85**, 633–662, https://doi.org/10.2151/jmsj.85.633.

Okabayashi, T., 1969: Photographs of heavy snowfall on the Japan Sea side on Jan. 2, 1969 (in Japanese). *Tenki*, **16**, 79–80.

——, and M. Satomi, 1971: A study on the snowfall and its original clouds by the meteorological radar and satellite (Part I) (in Japanese). *Tenki*, **18**, 573–581.

Passarelli, R. E., Jr., and R. R. Braham Jr., 1981: The role of the winter land breeze in the formation of Great Lake snow storms. *Bull. Amer. Meteor. Soc.*, **62**, 482–491, https://doi.org/10.1175/1520-0477(1981)062<0482:TROTWL>2.0.CO;2.

Rasmussen, E. A., and M. Lystad, 1987: The Norwegian Polar Lows Project: A summary of the International Conference on Polar Lows, 20–23 May 1986, Oslo, Norway. *Bull. Amer. Meteor. Soc.*, **68**, 801–816.

——, and J. Turner, 2003: *Polar Lows: Mesoscale Weather Systems in the Polar Regions.* Cambridge University Press, 612 pp., https://doi.org/10.1017/CBO9780511524974.

Reed, R. J., 1979: Cyclogenesis in polar airstreams. *Mon. Wea. Rev.*, **107**, 38–52, https://doi.org/10.1175/1520-0493(1979)107<0038:CIPAS>2.0.CO;2.

Saito, K., M. Murakami, T. Matsuo, and H. Mizuno, 1996: Sensitivity experiments on the orographic snowfall over the mountainous region of northern Japan. *J. Meteor. Soc. Japan*, **74**, 797–813, https://doi.org/10.2151/jmsj1965.74.6_797.

Sardie, J. M., and T. T. Warner, 1985: A numerical study of the development mechanisms of polar lows. *Tellus*, **37A**, 460–477, https://doi.org/10.1111/j.1600-0870.1985.tb00444.x.

Shimada, U., A. Wada, K. Yamazaki, and N. Kitabatake, 2014: Roles of an upper-level cold vortex and low-level baroclinicity in the development of polar lows over the Sea of Japan. *Tellus*, **66A**, 24694, https://doi.org/10.3402/tellusa.v66.24694.

Shinoda, Y., R. Kawamura, T. Kawano, and H. Shimizu, 2021: Dynamical role of the Changbai Mountains and the Korean Peninsula in the wintertime quasi-stationary convergence zone over the Sea of Japan. *Int. J. Climatol.*, **41** (Suppl. 1), E602–E615, https://doi.org/10.1002/joc.6713.

Skamarock, W. C., and J. B. Klemp, 2008: A time-split non-hydrostatic atmospheric model for weather research and forecasting applications. *J. Comput. Phys.*, **227**, 3465–3485, https://doi.org/10.1016/j.jcp.2007.01.037.

SSEC, 2018, University of Wisconsin–Madison Space Science and Engineering Center (SSEC) Multi-format Client-agnostic File Extraction Through Contextual HTTP (MCFETCH). Accessed 14 December 2019, https://mcfetch.ssec.wisc.edu/.

Steenburgh, W. J., 2014: *Secrets of the Greatest Snow on Earth.* Utah State University Press, 186 pp.

——, and L. S. Campbell, 2017: The OWLeS IOP2b lake-effect snowstorm: Shoreline geometry and the mesoscale forcing of precipitation. *Mon. Wea. Rev.*, **145**, 2421–2436, https://doi.org/10.1175/MWR-D-16-0460.1.

——, and S. Nakai, 2020: Perspectives on sea- and lake-effect precipitation from Japan's "Gosetsu Chitai". *Bull. Amer. Meteor. Soc.*, **101** (1), E58–E72, https://doi.org/10.1175/BAMS-D-18-0335.1.

——, S. F. Halvorson, and D. J. Onton, 2000: Climatology of lake-effect snowstorms of the Great Salt Lake. *Mon. Wea. Rev.*, **128**, 709–727, https://doi.org/10.1175/1520-0493(2000)128<0709:COLESO>2.0.CO;2.

Steiger, S. M., and Coauthors, 2013: Circulations, bounded weak echo regions, and horizontal vortices observed within long-lake-axis-parallel–lake-effect storms by the Doppler on Wheels. *Mon. Wea. Rev.*, **141**, 2821–2840, https://doi.org/10.1175/MWR-D-12-00226.1.

Takahashi, H. G., N. H. Ishizaki, H. Kawase, M. Hara, T. Yoshikane, X. Ma, and F. Kimura, 2013: Potential impact of sea surface temperature on winter precipitation over the Sea of Japan side of Japan: A regional climate modeling study. *J. Meteor. Soc. Japan*, **91**, 471–488, https://doi.org/10.2151/jmsj.2013-404.

Thompson, G., P. R. Field, R. M. Rasmussen, and W. D. Hall, 2008: Explicit forecasts of winter precipitation using an improved bulk microphysics scheme. Part II: Implementation of a new snow parameterization. *Mon. Wea. Rev.*, **136**, 5095–5114, https://doi.org/10.1175/2008MWR2387.1.

Tsuboki, K., and G. Wakahama, 1992: Mesoscale cyclogenesis in winter monsoon air streams: Quasi-geostrophic baroclinic instability as a mechanism of the cyclogenesis off the west coast of Hokkaido Island, Japan. *J. Meteor. Soc. Japan*, **70**, 77–93, https://doi.org/10.2151/jmsj1965.70.1_77.

——, and T. Asai, 2004: The multi-scale structure and development mechanism of mesoscale cyclones over the Sea of Japan in winter. *J. Meteor. Soc. Japan*, **82**, 597–621, https://doi.org/10.2151/jmsj.2004.597.

Tsuchiya, K., and T. Fujita, 1967: A satellite meteorological study of evaporation and cloud formation over the western Pacific under the influence of the winter monsoon. *J. Meteor. Soc. Japan*, **45**, 232–250, https://doi.org/10.2151/jmsj1965.45.3_232.

Uemura, H., 1980: On the structure and formation of the disturbances causing a heavy snowfall over the coastal area of the Sea of Japan under the winter monsoon (in Japanese). *Tenki*, **27**, 33–44.

Umek, L., and A. Gohm, 2016: Lake and orographic effects on a snowstorm at Lake Constance. *Mon. Wea. Rev.*, **144**, 4687–4707, https://doi.org/10.1175/MWR-D-16-0032.1.

University of Wyoming, 2018: University of Wyoming Department of Atmospheric Sciences Upper Air Sounding Data. Accessed 15 October 2018, http://weather.uwyo.edu/upperair/sounding.html.

Veals, P. G., and W. J. Steenburgh, 2015: Climatological characteristics and orographic enhancement of lake-effect precipitation east of Lake Ontario and over the Tug Hill Plateau. *Mon. Wea. Rev.*, **143**, 3591–3609, https://doi.org/10.1175/MWR-D-15-0009.1.

——, ——, S. Nakai, and S. Yamaguchi, 2019: Factors affecting the inland and orographic enhancement of sea-effect snowfall in the Hokuriku Region of Japan. *Mon. Wea. Rev.*, **147**, 3121–3143, https://doi.org/10.1175/MWR-D-19-0007.1.

——, ——, ——, and ——, 2020: Intrastorm variability of the inland and orographic enhancement of a sea-effect snowstorm in the Hokuriku Region of Japan. *Mon. Wea. Rev.*, **148**, 2527–2548, https://doi.org/10.1175/MWR-D-19-0390.1.

Watanabe, S. I., H. Niino, and W. Yanase, 2016: Climatology of polar mesocyclones over the Sea of Japan using a new objective tracking method. *Mon. Wea. Rev.*, **144**, 2503–2515, https://doi.org/10.1175/MWR-D-15-0349.1.

——, ——, and ——, 2018: Composite analysis of polar mesocyclones over the western part of the Sea of Japan. *Mon. Wea. Rev.*, **146**, 985–1004, https://doi.org/10.1175/MWR-D-17-0107.1.

West, T. K., W. J. Steenburgh, and G. G. Mace, 2019: Characteristics of sea-effect clouds and precipitation over the Sea of Japan region as observed by A-Train satellites. *J. Geophys. Res. Atmos.*, **124**, 1322–1335, https://doi.org/10.1029/2018JD029586.

Yamaguchi, K., and C. Magono, 1974: On the vortical disturbances in small scale accompanied with the mesoscale front in Japan Sea in winter season (in Japanese). *Tenki*, **21**, 83–88.

Yamaguchi, S., O. Abe, S. Nakai, and A. Sato, 2011: Recent fluctuations of meteorological and snow conditions in Japanese mountains. *Ann. Glaciol.*, **52**, 209–215, https://doi.org/10.3189/172756411797252266.

Yanase, W., H. Niino, and K. Saito, 2002: High-resolution numerical simulation of a polar low. *Geophys. Res. Lett.*, **29**, 3-1–3-4, https://doi.org/10.1029/2002GL014736.

——, ——, S. Watanabe, K. Hodges, M. Zahn, T. Spengler, and I. Gurvich, 2016: Climatology of polar lows over the Sea of Japan using the JRA-55 reanalysis. *J. Climate*, **29**, 419–437, https://doi.org/10.1175/JCLI-D-15-0291.1.

Yoshihara, H., M. Kawashima, K. I. Arai, J. Inoue, and Y. Fujiyoshi, 2004: Doppler radar study on the successive development of snowbands at a convergence line near the coastal region of Hokuriku District. *J. Meteor. Soc. Japan*, **82**, 1057–1079, https://doi.org/10.2151/jmsj.2004.1057.